Supporting Information

SUPPLEMENTARY MATERIAL

SI Methods

Multiple Sequence Alignment of Voltage-Gated Sodium and Potassium Channels. Sequence alignment between VSDs of the Na_V and K_V channels is well defined for the S1, S2, and S3 segments due to several highly conserved charged and/or polar residues (1) (Figs. S1–S4). N36 and E43 in S1, D60, E70, and R74 in S2, and N90 and D93 in S3 of NaChBac have identical or highly homologous residues within both channel families (Figs. S1–S4). However, despite the highly conserved positively charged residues in S4 segment, sequence alignment is challenging (Fig. S5) because of the different number of positively charged residues in different S4 segments (Figs. S1–S4). We used the HHPred homology detection server (2–4) and the X-ray structures of $K_V1.2$-$K_V2.1$ chimera (5), KvAP (6), and MlotiK1 (7) channels to generate a universal S4 alignment for Na_V and K_V channels (Figs. S1 and S5*B*). The alignment indicates that the S4 segment is formed by residues V109-V127 and the S4–S5 linker is formed by residues P128 to T140 in NaChBac. The gating-charge-carrying arginines in S4 of NaChBac (R1-R4) are aligned with R2-K5 in the $K_V1.2$ channel, and the position of the first arginine in the S4 segment of $K_V1.2$ (R0) is occupied by T110 in S4 of NaChBac (T0, Fig. S1). Alternative S4 alignments were also considered, but only the HHpred server-based method aligned all three of the large hydrophobic residues (indicated by asterisks in Figs. S1 and S5) that are important for interaction of the pore-lining S6 segment with the S4–S5 linker region (8). These residues have a high propensity to form turns at the *N*- and C-termini of the S4–S5 linker (P128, S129, T140, and P142 in NaChBac) that are aligned with S307 and S320 at the *N*- and C-terminal edges of the S4–S5 linker in the $K_V1.2$-$K_V2.1$ channel (5). We used this HHpred server-based S4 alignment to generate the majority of models presented in this paper, although we also used other S4 alignments to build models of deep resting states (see *Rosetta-Membrane Modeling of the Voltage-Sensing Domain of NaChBac* below) and to explore the extent of conversion of 3_{10}-helix to α-helix conversion in part of the S4 segment during gating (1, 5, 9–11).

Based on this HHpred alignment, we find that several amino acid residues are nearly 100% conserved within the VSDs of bacterial (Fig. S2) and human (Fig. S3) Na_V channel families, including I33 (in S1), E70 (in S2), W89 and D93 (in S3), and R1, R2, and R3 (in S4). Charged or polar amino acids are relatively highly conserved at positions N36 and E43 (in S1), D60 and K74 (in S2), N90 (in S3), and R4 and S125 (in S4). Several hydrophobic amino acids are highly conserved in the center of the transmembrane segments at positions I29 (in S1), F67 (in S2), and V97 (in S3) (Figs. S2 and S3). These three sets of highly conserved amino acid residues are likely to be essential for the structure and function of all voltage sensors. On the other hand, several amino acid residues are highly conserved in either bacterial or human Na_V channels, but not in both (Figs. S2 and S3, and legend to Fig. S2). We suggest that these differences in conservation profiles between bacterial and human Na_V channel families may reflect evolutionary fine-tuning of the voltage-gating mechanism in Na_V channels.

Full-Atom Rosetta-Membrane Method. A modified version of the Rosetta-Membrane full-atom method (12) was developed that incorporated the following changes in energy function and protocol. A coarse-grained membrane environment energy term was added to the energy function and derived from statistical analysis of nonhomologous set of membrane protein structures (13). Relative weights of hydrogen bonding energies between side chain–side chain and side chain–backbone atoms were increased by a factor of 2 in the Rosetta-Membrane full-atom energy function. Membrane normal and center searches were conducted before the full-atom conformational search.

Rosetta-Membrane Modeling of the Voltage-Sensing Domain of NaChBac. Homology, *de novo,* and full-atom modeling of the VSD of NaChBac was performed using the Rosetta-Membrane (12–14) and Rosetta symmetry (15) methods. The pore-forming domain (PD) and S4–S5 linker structure of the $K_V1.2$-$K_V2.1$ chimera (5) channel were used to generate PD and S4–S5 linker model of $K_V1.2$-$K_V2.1$ structure based and all activated states of NaChBac using the HHpred server based alignment shown in Figs. S1 and S5*B*. The PD and S4–S5 linker structures of the MlotiK1 (7) channel were used to generate the PD and S4–S5 linker models of all resting states of NaChBac using the HHpred-based alignment shown in Figs. S1 and S5*B*. The selectivity filter region (between the P-helix and S6 segment) was excluded from modeling of all PD states because of the focus of this paper on the VSD. The S4 segment was moved one helical turn up or down starting from the HHPred-based sequence alignment (Fig. S1) to generate S4 models with different starting and ending positions of 3_{10}-helix structure (Fig. S5). The Rosetta-Membrane homology method was used to generate models of NaChBac in which the backbone structure of the transmembrane regions and intracellular S2–S3 loop were built based on $K_V1.2$-$K_V2.1$ chimera template and S1-S2 and S3-S4 loops were built de novo. The NaChBac model based on the $K_V1.2$-$K_V2.1$ channel chimera structure (Fig. 1) was built without any experimental constraints and was based on sequence alignment shown in Figs. S1 and S5*B*. All other NaChBac models were generated using Rosetta-Membrane-Symmetry full-atom relax protocol (12–15) starting from $K_V1.2$-$K_V2.1$ chimera-based models of VSD connected to $K_V1.2$-$K_V2.1$ chimera and MlotiK1 channels based homology models of S4–S5 linker and PD (see above) and using distance constraints based on experimental data (see Table S6). Different S4 alignments between NaChBac and the $K_V1.2$-$K_V2.1$ chimera were considered when building preliminary models of multiple states of VSD of NaChBac (Fig. S5). The HHpred-based S4 alignment (Figs. S1 and S5*B*) satisfied the majority of experimental data for all activated states and *Resting State 3* (see Table S3). The S4 alignment where R1 in NaChBac is aligned with R3 in the $K_V1.2$-$K_V2.1$ chimera (Fig. S5*C*) satisfied the majority of experimental data for the *Resting States 1* and *2* (see Table S3). Other S4 alignments (Fig. S5 *A* and *D*) generated models where the C-terminal end of S4 had significant changes in secondary structure (for models of the activated states) or extensive backbone clashes with the N-terminal end of the S4–S5 linker (for models of the resting states) and therefore have not been used as templates for any of the models presented in this paper. The S3–S4 loop and the S4–S5 linker were generated de novo for the starting template based on the S4 alignment shown in Fig. S5*C*. 10,000 models were generated for each constraint and the ten lowest energy models were then used as input to symmetric membrane full atom relax protocol without any experimental constraints. The ten lowest-energy models were chosen as the best models for each of the VSD states. All structural figures in the paper were generated using the UCSF Chimera package (16).

Electrophysiology and Disulfide Locking. Cells were seeded onto glass coverslips and placed in perfusion chamber for experiments. Extracellular solution contained (in mM) NaCl (150), $CaCl_2$ (1.5), $MgCl_2$ (1), KCl (2), glucose (10), Hepes (10) (pH 7.4). The intracellular (pipette) solution contained (in mM) CsF (105), EGTA (10), NaCl (35), Mg-ATP (4), Hepes (10) (pH 7.4). Oxidizing agent hydrogen peroxide (H_2O_2) and reducing agents βME and Tris(2-carboxyethyl)phosphine (TCEP) were added to the extracellular solution at the final concentrations as indicated and used within twenty min. For experiments using oxidizing agents and reducing agents, cells were continuously perfused with extracellular solution (2-3 mL/min). Steady-state effects for induction or reversal of disulfide locking were achieved after 3–5 min of exposure to reagents and were monitored by recording changes in I_{Na} during 500 ms pulses to 0 mV from a holding potential of -140 mV applied at 0.1 Hz. Percent disulfide locked channels in the activated state were measured by percentage of the normalized I_{Na} lost after the first pulse in control or in the presence of 10 mM H_2O_2. Percent disulfide locked channels in the deactivated state was measured by percentage of the normalized I_{Na} recovered after 4 min extracellular application of 10 mM βME.

Mutant Cycle Analysis. The voltage dependence of activation was characterized using fits of $(V\text{-}V_{Rev})/1+\exp[(V\text{-}V_{1/2})/k$ to current-voltage relationships, where V_{Rev} was the extrapolated reversal potential, $V_{1/2}$ the half activation voltage, and, k, a slope factor equal to RT/ZF; Z was the apparent gating charge. The parameter Z was determined from fits to current-voltage relationships as described above. The amount of free energy required to shift the channel from the closed to the open state was calculated as $\Delta G^\circ_{C\rightarrow O}$ (kcal/mol) = $23.06ZV_{1/2}$, where $V_{1/2}$ was the half activation voltage. The perturbation in free energy of the mutant channel relative to the wild-type was calculated as $\Delta\Delta G^\circ = \Delta(ZV_{1/2}) = 23.06[Z_{mut}V_{1/2mut} - Z_{wt}V_{1/2wt}]$. Coupling of nonadditive free energy was calculated as $\Sigma\Delta G^\circ_{coupled} = \Delta\Delta G^\circ_{Mut1:Mut2} - (\Delta\Delta G^\circ_{Mut1} + \Delta\Delta G^\circ_{Mut2})$.

SI Results

Comparison with the NavAb Channel. The structure of the VSD of NaChBac determined by structural modeling in this work and the structure of the voltage sensor of NavAb determined by X-ray crystallography are very similar. Approximately 80% of residues within S1-S4 transmembrane segments are superimposed within ~1.5 Å root-mean-square deviation (RMSD) between Cα atoms, except for the N-terminal end of S1 which is untethered in our structures and therefore in a significantly different position than in NavAb (Fig. S6). This close agreement between the Rosetta structural model of the NaChBac voltage sensor and the X-ray structure of the voltage sensor of NavAb (Fig. S6) suggests that our structural models developed using the Rosetta-Membrane-Symmetry method will have relevance for the function of voltage sensors of Na_V and K_V channels in general.

Modeling Further Activated States. Structural modeling with the Rosetta-Membrane method does not take account of membrane potential because there is no method available to define the shape of the electric field within the voltage sensor. Nevertheless, the conformation of the VSD is voltage-sensitive and must be influenced by changes in membrane potential. Although the VSD is activated at 0 mV, it is possible that the most fully activated conformations of the VSD are only stable at positive membrane potentials. We explored the possibility of a further activated state based on interaction of R3 with E43 (in S1), as suggested by state-dependent disulfide-crosslinking data (17). Constraining R3 interaction with E43 (in S1) formed new ionic interactions and hydrogen bonds without any significant effect on the secondary structure of the VSD segments; however, relaxing these models without constraints broke those hydrogen bonds and allowed the R3 side chain to move inward to form interactions with N36 (in S1) and D60 (in S2) in all 10 lowest energy models (Fig. S7, E43-R3). This result suggests that an activated state with an ion pair between E43 and R3 is not stable without an externally applied positive transmembrane potential. These results from structural modeling are consistent with the disulfide-locking experiments because the interaction of R3 with E43 required a stronger depolarization and longer time to form than the interactions that lead to *Activated States 1–3* (17). Thus, the disulfide-locking data suggest that one or more additional activated states may exist at more positive membrane potentials but are not stable in our models because no membrane potential term has been applied in our modeling algorithm.

Modeling Deeper Resting States. Because structural modeling with the Rosetta-Membrane method does not take account of the membrane potential, we expect that the deepest resting states that require very negative membrane potentials in vivo would not be stable in our modeling protocol without applying an additional force like a distance constraint. We attempted to build VSD models of deeper resting states using distance constraints suggested by the results of Tao et al. (18) and previously modeled by Shafrir et al. (1), where R1 or R2 would interact with the intracellular negative charge cluster (Fig. S9). Constraining R1 interaction with E70 (in S2) generated models that significantly bent the S2 helix in the intracellular and extracellular regions and the S4 helix in the extracellular region (Fig. S9, E70-R1). These extensive secondary structure changes are not expected based on the absence of residues with high propensity to form helix bends in those regions of S2 and S4 and suggest that R1-E70 interaction is unlikely to form in the NaChBac VSD, except perhaps under the influence of large electrical fields. Constraining R2 interaction with E70 (in S2) formed new ionic interactions and hydrogen bonds without any significant effect on secondary structure of VSD segments; however, relaxing these models without any constraints broke those hydrogen bonds and allowed the R2 side chain to move to the extracellular side of the HCS in 9 out of 10 lowest energy models (Fig. S9, E70-R2). These results indicate that hydrogen bonds between E70 and R2 are not stable without a strongly hyperpolarized voltage applied to the membrane.

Disulfide Locking of D60C with T0C, R1C, and R2C. We predicted that these double-cysteine mutants would form disulfide bonds in the resting state, which would prevent their activation until the disulfide bonds were reduced. As expected, these double-cysteine mutants do not conduct measurable sodium current when expressed by transfection in embryonic kidney tsA-201 cells or by baculloviral infection in *Drosophila* Hi5 cells, whereas the single mutant channels have normal function (Fig. S11). Unfortunately, no Na^+ current is rescued by reduction of disulfide bonds with sulfhydryl reagents, in contrast to expectations (Fig. S11). On the other hand, the double mutants D60C:T0A, D60C:R1A and D60C:R2A were functionally expressed in both tsA-201 and Hi5 cells (Fig. S11). Moreover, coexpression of D60C:R1C or D60C:R2C with a covalently connected trimer of wild-type NaChBac subunits rescued some Na^+ current (Fig. S11). However, the functional effects of depolarizing pulses and disulfide reagents on these heteromeric channels were small and inconsistent, probably because only one of the four NaChBac subunits contained paired-cysteine substitutions and was able to undergo disulfide locking and unlocking. Localization of eGFP-tagged NaChBac channels by confocal microscopy indicated that the double-

cysteine mutants D60C:T0C, D60C:R1C and D60C:R2C are sequestered in intracellular inclusions, whereas wild-type, single-cysteine mutations, and the double-mutants D60C:T0A, D60C:R1A and D60C:R2A channels are partially translocated to the cell surface, in addition to having a substantial pool of channels remaining in the endoplasmic reticulum (Fig. S12). These results suggest that the double-cysteine mutants D60C:T0C, D60C:R1C and D60C:R2C form disulfide bonds that are recognized as improperly assembled and sequestered before translocation to the cell surface, whereas single cysteine mutants are expressed normally.

Specificity of Disulfide Locking and Energy Coupling. The X-ray crystal structures of the K_VAP (5) and the $K_V1.2$-$K_V2.1$ chimera (8), as well as the Rosetta model of NaChBac (Fig. 1), show the side chain from residue D60 or its equivalent facing into the gating pore toward the S4 segment. In contrast, the side chain of the adjacent residue I59 faces away from the gating pore and into the surrounding lipid in all three structures. These structures predict that a cysteine in the position of I59 would not interact with V109, T0, L112 or gating charges R1-R4 in the resting state. To test the possibility that this neighboring amino acid residue of I59 might form disulfide bonds nonspecifically with cysteines substituted for gating charges in the S4 segment, we studied double cysteine mutants I59C:V109C, I59C:T0C, I59C:L112C, I59C:R1C, I59C:R2C, I59C:R3C and I59C:R4C. We found no evidence for state-dependent disulfide locking of any of these pairs of substituted cysteine residues, supporting the specificity of disulfide locking of amino acid residues whose native side chains would form ion pairs during activation of the voltage sensor (Fig. S14 and Table S3). Moreover, we found no energy coupling between I59C and any R4 cysteines except for R2C in mutant cycle analysis (Fig. S14). These results provide strong support for the specificity of sulfhydryl interactions of D60C with V109C, L112C, R3C, and R4C.

SI Discussion

Implications of the 3_{10} Helical Structure of the S4 Segment. The X-ray crystal structures of the S4 segments in the voltage sensors of the K_VAP channel and the $K_V1.2$ channel are fully in alpha-helical conformation (6, 8, 19). In contrast, the S4 segment of the $K_V1.2$- $K_V2.1$ channel chimera has a 3_{10} helical conformation over the portion of the S4 segment from gating charge R3 to the inner end of the S4 helix in its activated state (5, 6), and the S4 segment in the X-ray crystal structure of the closed state of the related MlotiK cyclic nucleotide-gated channel, which is not voltage-gated, has the 3_{10} conformation throughout its length (20). The VSD of the NavAb bacterial sodium channel also has its S4 segment fully in the 3_{10}-helical conformation from R1 to R4 in an activated state (21). Taken together, these structural studies support the possibility that the S4 segment can adopt different mixtures of alpha-helical and 3_{10}-helical structures in different functional states. 3_{10} helices are uncommon in proteins (22) and are usually found in short stretches of sequence, often as the terminating segment of an alpha helix (23). 3_{10} helices are considered less stable than alpha helices in aqueous environment (24), but the structure of amphipathic 3_{10} helices can be stabilized in lipid membrane environments by hydrophobic interactions (25). The 3_{10}-helix may also serve as a protein-folding intermediate leading to alpha helices (23, 26–28). Because each amino acid residue projects over a larger distance in a 3_{10} structure (~2 Å per helical turn) compared with an alpha helix (~1.5 Å per helical turn), and the side chains from amino acids in a 3_{10} helix radiate from the helix backbone at ~120° angles (~3 residues per turn) while side chains from alpha helices radiate at ~100° angles (~3.6 residues per turn). The 120° angle places the side chains of residues positioned at three-residue intervals in register along the axis of the 3_{10} helix, instead of in a spiral pattern as in alpha helices (Fig. S19). This structure would allow the gating charges positioned at three-residue intervals along the S4 segment to slide in a line past their ion pair partners for at least part of their movement through the gating pore. An additional possible function for the transition from 3_{10}-helix to alpha-helix is to release energy to drive pore opening. Voltage-driven outward movement of the S4 segment in the 3_{10}-conformation is supported by the finding that the entire S4 segment from R1-R4 is in the 3_{10} helical conformation in the structure of NavAb in its preopen state (21). This would have the effect of conserving some of the energy of the electric field in the 3_{10} conformation. Subsequent rewinding of the extracellular part of the S4 segment would be an energy-yielding conformational change that would drive concerting opening of the pore. Consistent with this idea, the open state of the $K_V1.2$ channel has significantly less of its S4 segment in the 3_{10} conformation (5, 8).

1. Shafrir Y, Durell SR, Guy HR (2008) Models of voltage-dependent conformational changes in NaChBac channels. *Biophys J* 95:3663–3676.
2. Söding J (2005) Protein homology detection by HMM-HMM comparison. *Bioinformatics* 21:951–960.
3. Söding J, Biegert A, Lupas AN (2005) The HHpred interactive server for protein homology detection and structure prediction. *Nucleic Acids Res* 33(Web Server issue):W244-8.
4. Hildebrand A, Remmert M, Biegert A, Söding J (2009) Fast and accurate automatic structure prediction with HHpred. *Proteins* 77(Suppl 9):128–132.
5. Long SB, Tao X, Campbell EB, MacKinnon R (2007) Atomic structure of a voltage-dependent K^+ channel in a lipid membrane-like environment. *Nature* 450:376–382.
6. Jiang Y, et al. (2003) X-ray structure of a voltage-dependent K+ channel. *Nature* 423:33–41.
7. Clayton GM, Altieri S, Heginbotham L, Unger VM, Morais-Cabral JH (2008) Structure of the transmembrane regions of a bacterial cyclic nucleotide-regulated channel. *Proc Natl Acad Sci USA* 105:1511–1515.
8. Long SB, Campbell EB, Mackinnon R (2005) Crystal structure of a mammalian voltage-dependent Shaker family K^+ channel. *Science* 309:897–903.
9. Catterall WA (2010) Ion channel voltage sensors: structure, function, and pathophysiology. *Neuron* 67:915–928.
10. Vieira-Pires RS, Morais-Cabral JH (2010) $3_{(10)}$ helices in channels and other membrane proteins. *J Gen Physiol* 136:585–592.
11. Khalili-Araghi F, et al. (2010) Calculation of the gating charge for the Kv1.2 voltage-activated potassium channel. *Biophys J* 98:2189–2198.
12. Barth P, Schonbrun J, Baker D (2007) Toward high-resolution prediction and design of transmembrane helical protein structures. *Proc Natl Acad Sci USA* 104:15682–15687.
13. Yarov-Yarovoy V, Schonbrun J, Baker D (2006) Multipass membrane protein structure prediction using Rosetta. *Proteins* 62:1010–1025.
14. Yarov-Yarovoy V, Baker D, Catterall WA (2006) Voltage sensor conformations in the open and closed states in ROSETTA structural models of K(+) channels. *Proc Natl Acad Sci USA* 103: 7292–7297.
15. André I, Bradley P, Wang C, Baker D (2007) Prediction of the structure of symmetrical protein assemblies. *Proc Natl Acad Sci USA* 104:17656–17661.
16. Pettersen EF, et al. (2004) UCSF Chimera—a visualization system for exploratory research and analysis. *J Comput Chem* 25:1605–1612.
17. DeCaen PG, Yarov-Yarovoy V, Scheuer T, Catterall WA (2011) Gating charge interactions with the S1 segment during activation of a Na^+ channel voltage sensor. *Proc Natl Acad Sci USA* 108:18825–18830.
18. Tao X, Lee A, Limapichat W, Dougherty DA, MacKinnon R (2010) A gating charge transfer center in voltage sensors. *Science* 328:67–73.
19. Long SB, Campbell EB, Mackinnon R (2005) Voltage sensor of Kv1.2: structural basis of electromechanical coupling. *Science* 309:903–908.
20. Clayton GM, Altieri S, Heginbotham L, Unger VM, Morais-Cabral JH (2008) Structure of the transmembrane regions of a bacterial cyclic nucleotide-regulated channel. *Proc Natl Acad Sci USA* 105:1511–1515.
21. Payandeh J, Scheuer T, Zheng N, Catterall WA (2011) The crystal structure of a voltage-gated sodium channel. *Nature* 475:353–358.
22. Barlow DJ, Thornton JM (1988) Helix geometry in proteins. *J Mol Biol* 201:601–619.
23. Banfield MJ, et al. (2001) Specificity in Trk receptor:neurotrophin interactions: the crystal structure of TrkB-d5 in complex with neurotrophin-4/5. *Structure* 9:1191–1199.
24. Walsh ST, et al. (2003) The hydration of amides in helices; a comprehensive picture from molecular dynamics, IR, and NMR. *Protein Sci* 12:520–531.
25. McDonnell PA, Shon K, Kim Y, Opella SJ (1993) fd coat protein structure in membrane environments. *J Mol Biol* 233:447–463.
26. Gerstein M, Chothia C (1991) Analysis of protein loop closure. Two types of hinges produce one motion in lactate dehydrogenase. *J Mol Biol* 220:133–149.

27. McPhalen CA, et al. (1992) Domain closure in mitochondrial aspartate aminotransferase. *J Mol Biol* 227:197–213.
28. Anderson TA, Cordes MH, Sauer RT (2005) Sequence determinants of a conformational switch in a protein structure. *Proc Natl Acad Sci USA* 102:18344–18349.
29. Clamp M, Cuff J, Searle SM, Barton GJ (2004) The Jalview Java alignment. *Bioinformatics* 20:426–427.
30. Waterhouse AM, Procter JB, Martin DM, Clamp M, Barton GJ (2009) Jalview Version 2—a multiple sequence alignment. analysis workbench. *Bioinformatics* 25:1189–1191.
31. Crooks GE, Hon G, Chandonia JM, Brenner SE (2004) WebLogo: a sequence logo generator. *Genome Res* 14:1188–1190.
32. Schneider TD, Stephens RM (1990) Sequence logos: a new way to display consensus sequences. *Nucleic Acids Res* 18:6097–6100.
33. Chakrapani S, Sompornpisut P, Intharathep P, Roux B, Perozo E (2010) The activated state of a sodium channel voltage sensor in a membrane environment. *Proc Natl Acad Sci USA* 107: 5435–5440.
34. Ruta V, Chen J, MacKinnon R (2005) Calibrated measurement of gating-charge arginine displacement in the KvAP voltage-dependent K^+ channel. *Cell* 123:463–475.
35. Campos FV, Chanda B, Roux B, Bezanilla F (2007) Two atomic constraints unambiguously position the S4 segment relative to S1 and S2 segments in the closed state of Shaker K channel. *Proc Natl Acad Sci U S A*.
36. Tombola F, Pathak MM, Gorostiza P, Isacoff EY (2007) The twisted ion-permeation pathway of a resting voltage-sensing domain. *Nature* 445:546–549.
37. Tombola F, Pathak MM, Isacoff EY (2005) Voltage-sensing arginines in a potassium channel permeate and occlude cation-selective pores. *Neuron* 45:379–388.
38. Sokolov S, Scheuer T, Catterall WA (2005) Ion permeation through a voltage- sensitive gating pore in brain sodium channels having voltage sensor mutations. *Neuron* 47:183–189.
39. Gamal El-Din TM, Heldstab H, Lehmann C, Greeff NG (2010) Double gaps along Shaker S4 demonstrate omega currents at three different closed states. *Channels (Austin)* 4:93–100.
40. Papazian DM, et al. (1995) Electrostatic interactions of S4 voltage sensor in Shaker K^+ channel. *Neuron* 14:1293–1301.
41. Broomand A, Elinder F (2008) Large-scale movement within the voltage-sensor paddle of a potassium channel-support for a helical-screw motion. *Neuron* 59:770–777.
42. Lin MC, Abramson J, Papazian DM (2010) Transfer of ion binding site from ether-a-go-go to Shaker: Mg^{2+} binds to resting state to modulate channel opening. *J Gen Physiol* 135: 415–431.
43. Paldi T, Gurevitz M (2010) Coupling between residues on S4 and S1 defines the voltage-sensor resting conformation in NaChBac. *Biophys J* 99:456–463.
44. Tiwari-Woodruff SK, Lin MA, Schulteis CT, Papazian DM (2000) Voltage-dependent structural interactions in the Shaker K(+) channel. *J Gen Physiol* 115:123–138.
45. Tiwari-Woodruff SK, Schulteis CT, Mock AF, Papazian DM (1997) Electrostatic interactions between transmembrane segments mediate folding of Shaker K^+ channel subunits. *Biophys J* 72:1489–1500.
46. DeCaen PG, Yarov-Yarovoy V, Sharp EM, Scheuer T, Catterall WA (2009) Sequential formation of ion pairs during activation of a sodium channel voltage sensor. *Proc Natl Acad Sci USA* 106:22498–22503.
47. DeCaen PG, Yarov-Yarovoy V, Zhao Y, Scheuer T, Catterall WA (2008) Disulfide locking a sodium channel voltage sensor reveals ion pair formation during activation. *Proc Natl Acad Sci USA* 105:15142–15147.
48. DeCaen PG, Yarov-Yarovoy V, Scheuer T, Catterall WA (2011) Molecular interactions during activation of a sodium channel voltage sensor.submitted.
49. Jiang Y, Ruta V, Chen J, Lee A, MacKinnon R (2003) The principle of gating charge movement in a voltage-dependent K+ channel. *Nature* 423:42–48.

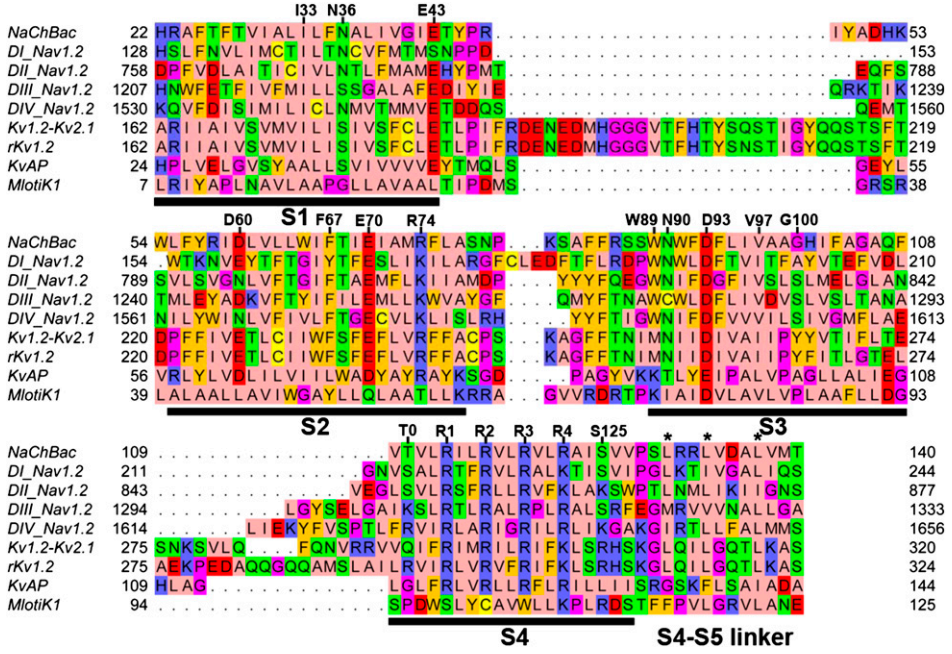

Fig. S1. Multiple sequence alignment of representatives of the voltage-gated sodium and potassium channel families. The amino acid sequence alignment of the VSDs of NaChBac, four domains of Nav1.2 channel (named from DI through DIV), Kv1.2-Kv2., Kv1.2, KvAP, and MlotiK1. Transmembrane segments from S1 through S4 are underlined by black bars and labeled. Positions of the gating charge carrying arginines in S4 and highly conserved residues in S1, S2, S3, and S4 segments are marked by a black line and labeled. Highly conserved hydrophobic residues in the S4–S5 linker are marked by asterisks. Amino acids were colored with Jalview program (29, 30) using the Zappo color scheme, where hydrophobic residues (I, L, V, A, and M) are colored pink, aromatic residues (F, W, and Y) are colored orange, positively charged residues (K, R, and H) are colored blue, negatively charged residues (D and E) are colored red, hydrophilic residues (S, T, N, and Q) are colored green, P and G colored magenta, and C is colored yellow.

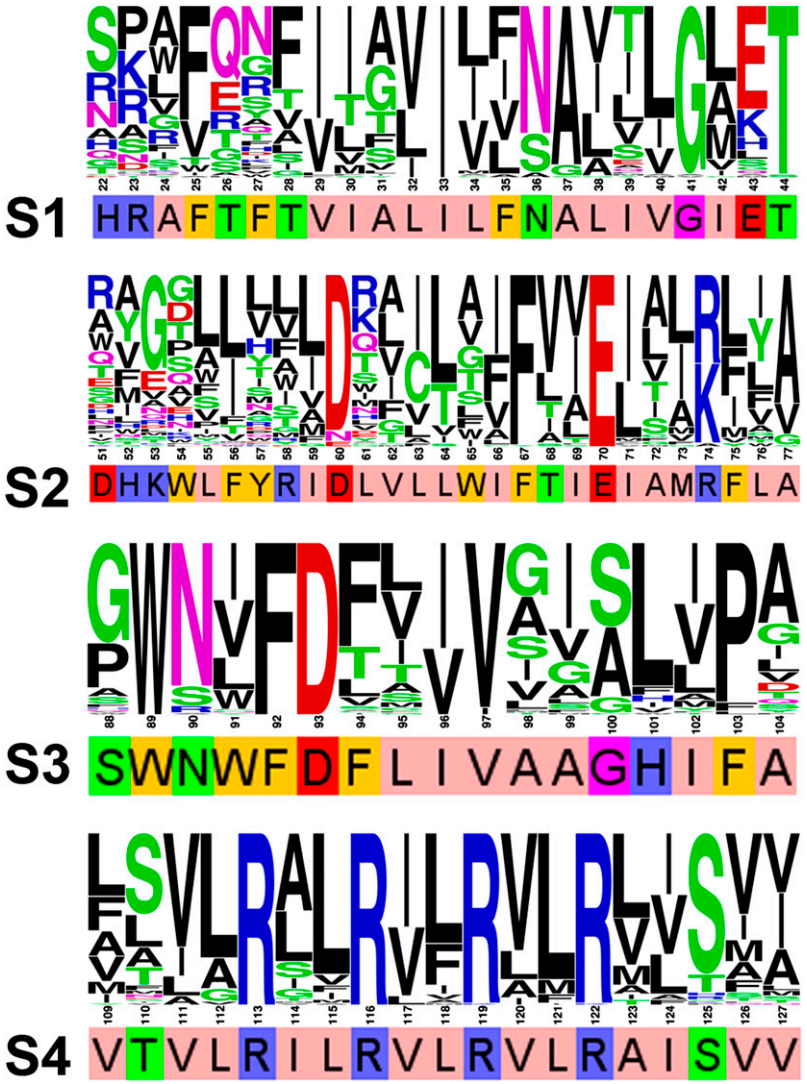

Fig. S2. Sequence conservation within the VSD of bacterial voltage-gated sodium channels. Amino acid conservation within VSD transmembrane segments of bacterial Nav channels represented as sequence logo generated using WebLogo server (31, 32). NaChBac sequence for each transmembrane segment shown as a reference with individual residues and transmembrane regions numbered and labeled accordingly. Height of individual amino acid at each position indicates its propensity at that position.

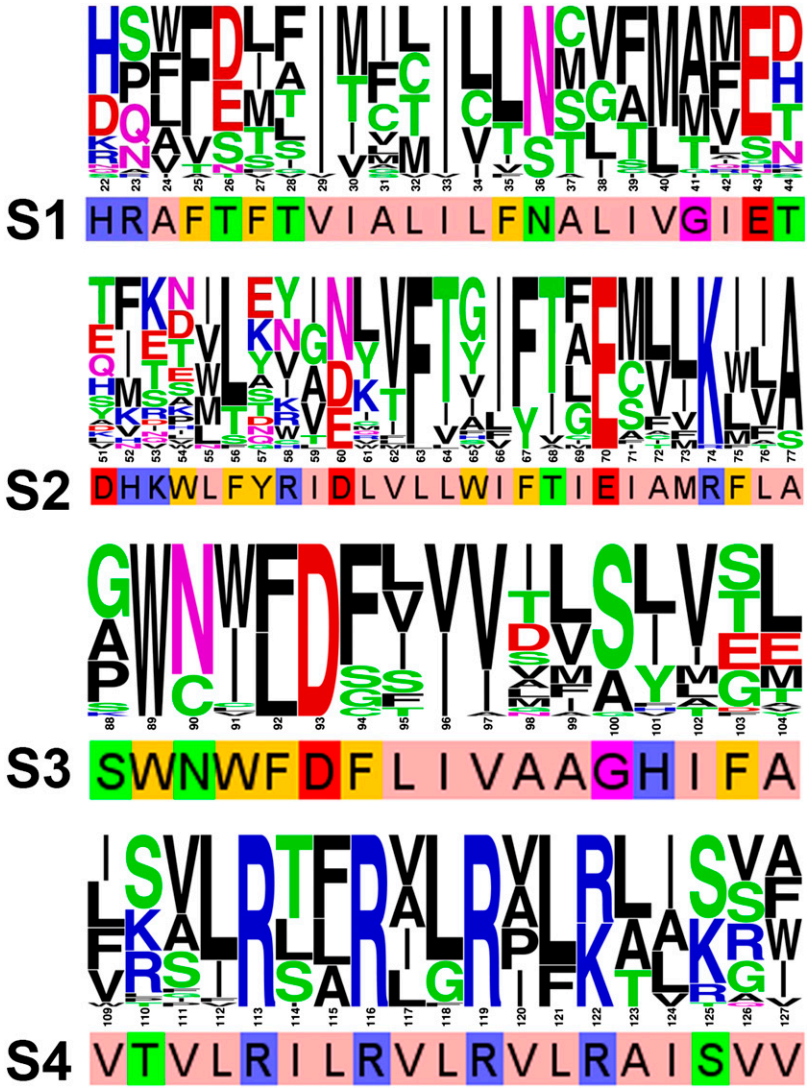

Fig. S3. Sequence conservation within the VSD of human voltage-gated sodium channels. Amino acid conservation within VSD transmembrane segments of human Nav channels represented as sequence logo generated using WebLogo server (31, 32). NaChBac sequence for each transmembrane segment shown as a reference with individual residues and transmembrane regions numbered and labeled accordingly. Height of individual amino acid at each position indicates its propensity at that position.

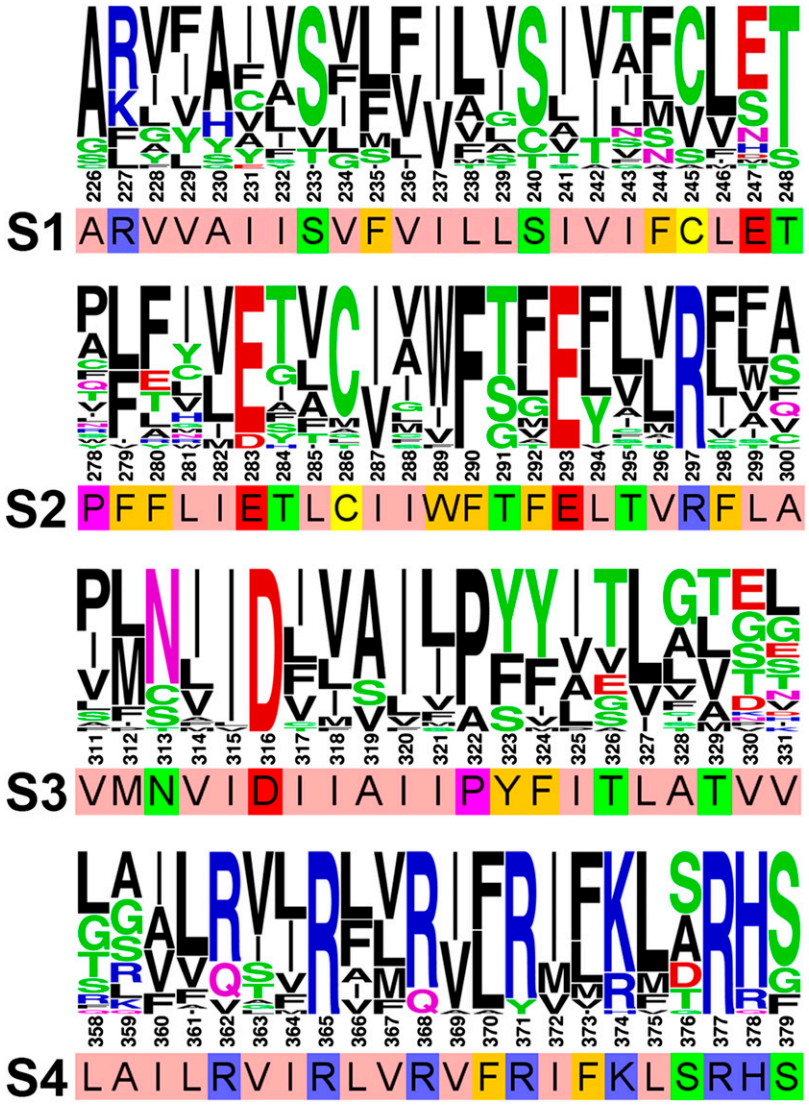

Fig. S4. Sequence conservation within VSD of human voltage-gated potassium channels. Amino acid conservation within VSD transmembrane segments of human Kv1-9 channels represented as sequence logo generated using WebLogo server (31, 32). Kv10-12 channels were excluded from this analysis because they have significantly shorter S4–S5 linker and contain a number of significantly different highly conserved residues compared with Kv1-9 channels. Shaker Kv channel sequence for each transmembrane segment shown as a reference with individual residues and transmembrane regions numbered and labeled accordingly. Height of individual amino acid at each position indicates its propensity at that position.

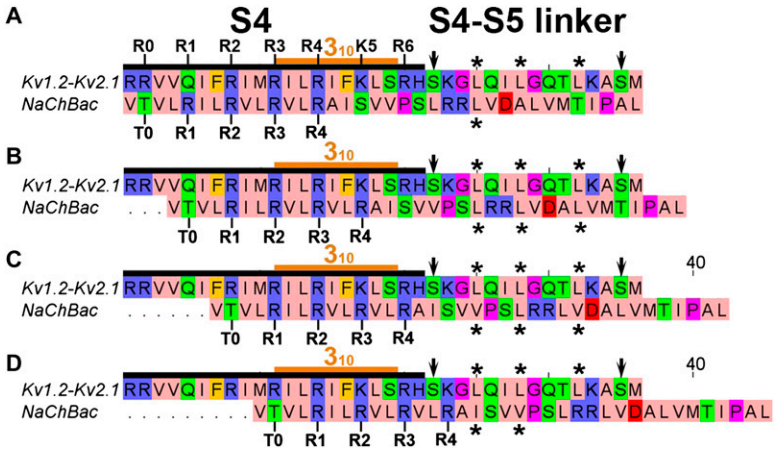

Fig. S5. Sequence alignment of S4 segments of NaChBac and the $K_V1.2$-$K_V2.1$ chimera. (*A*) Alignment of S4 of NaChBac to Kv1.2-Kv2.1 chimera shifted by 3 positions to the left relative to HHPred server based alignment (see Fig. S1). (*B*) HHPred server based alignment between S4 of NaChBac to Kv1.2-Kv2.1 chimera (see Fig. S1). (*C*) Alignment of S4 of NaChBac to Kv1.2-Kv2.1 chimera shifted by 3 positions to the right relative to HHPred server based alignment (see Fig. S1). (*D*) Alignment of S4 of NaChBac to Kv1.2-Kv2.1 chimera shifted by 6 positions to the right relative to HHPred server based alignment (see Fig. S1). Positions of the gating charge carrying arginines in S4 and other key residues are marked by a black line and labeled. Highly conserved large hydrophobic residues in the S4–S5 linker are marked by asterisks. Positions of S307 and S320 that form the *N*- and C-termini edges of the S4–S5 linker in the X-ray structure of Kv1.2-Kv2.1 channel (5) indicated by arrows. Amino acids were colored with Jalview program (29, 30) using the Zappo color scheme, where hydrophobic residues (I, L, V, A, and M) are colored pink, aromatic residues (F, W, and Y) are colored orange, positively charged residues (K, R, and H) are colored blue, negatively charged residues (D and E) are colored red, hydrophilic residues (S, T, N, and Q) are colored green, P and G colored magenta, and C is colored yellow.

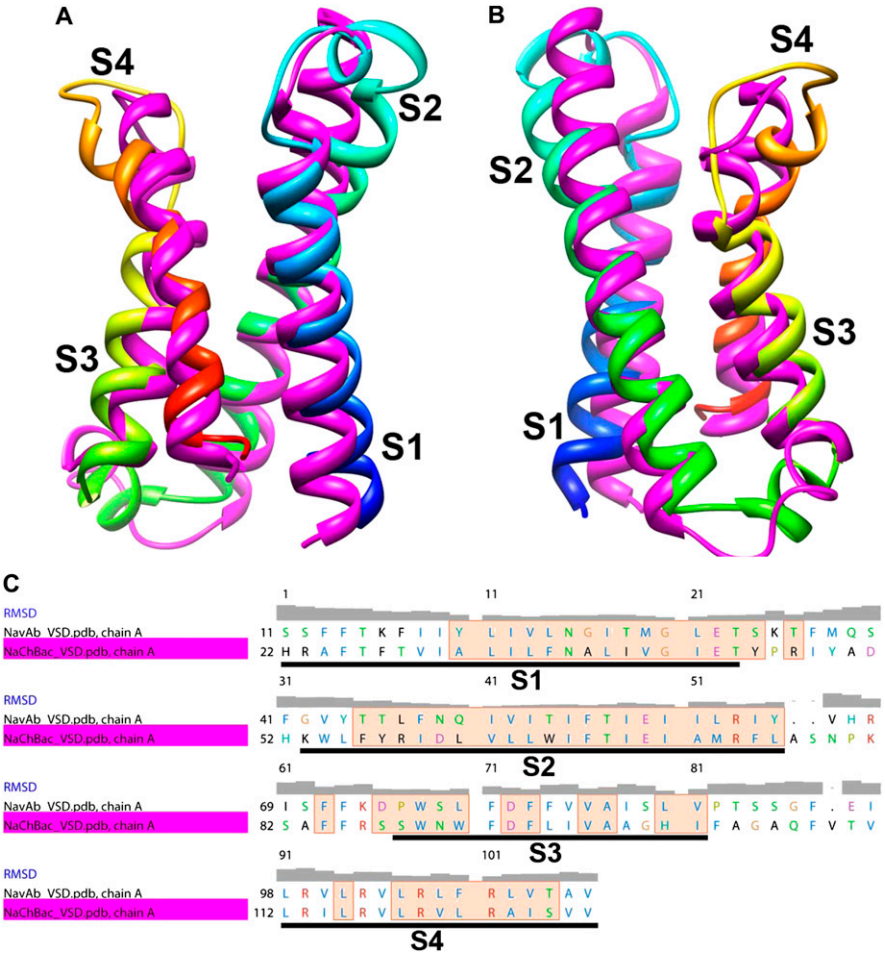

Fig. S6. Comparison of the Rosetta model of the VSD of NaChBac and the X-ray structure of the VSD of NavAb. (*A*) Transmembrane view of superposition of VSDs of Kv1.2-Kv2.1 based model of NaChBac (colored magenta) and the X-ray structure of NavAb (21) (colored by rainbow scheme from blue (S1) to green (S2) to yellow (S3) to red (S4)) with segments S1 and S4 at the front as labeled. (*B*) View of superposition of VSDs shown in panel *A* with segments S2 and S3 at the front as labeled. (*C*) Structure based sequence alignment of the VSDs of the Kv1.2-Kv2.1 based model of NaChBac and the X-ray structure of NavAb with sequence regions that superimposed within ~1.5 Å RMSD threshold highlighted by pink color and enclosed in orange boxes.

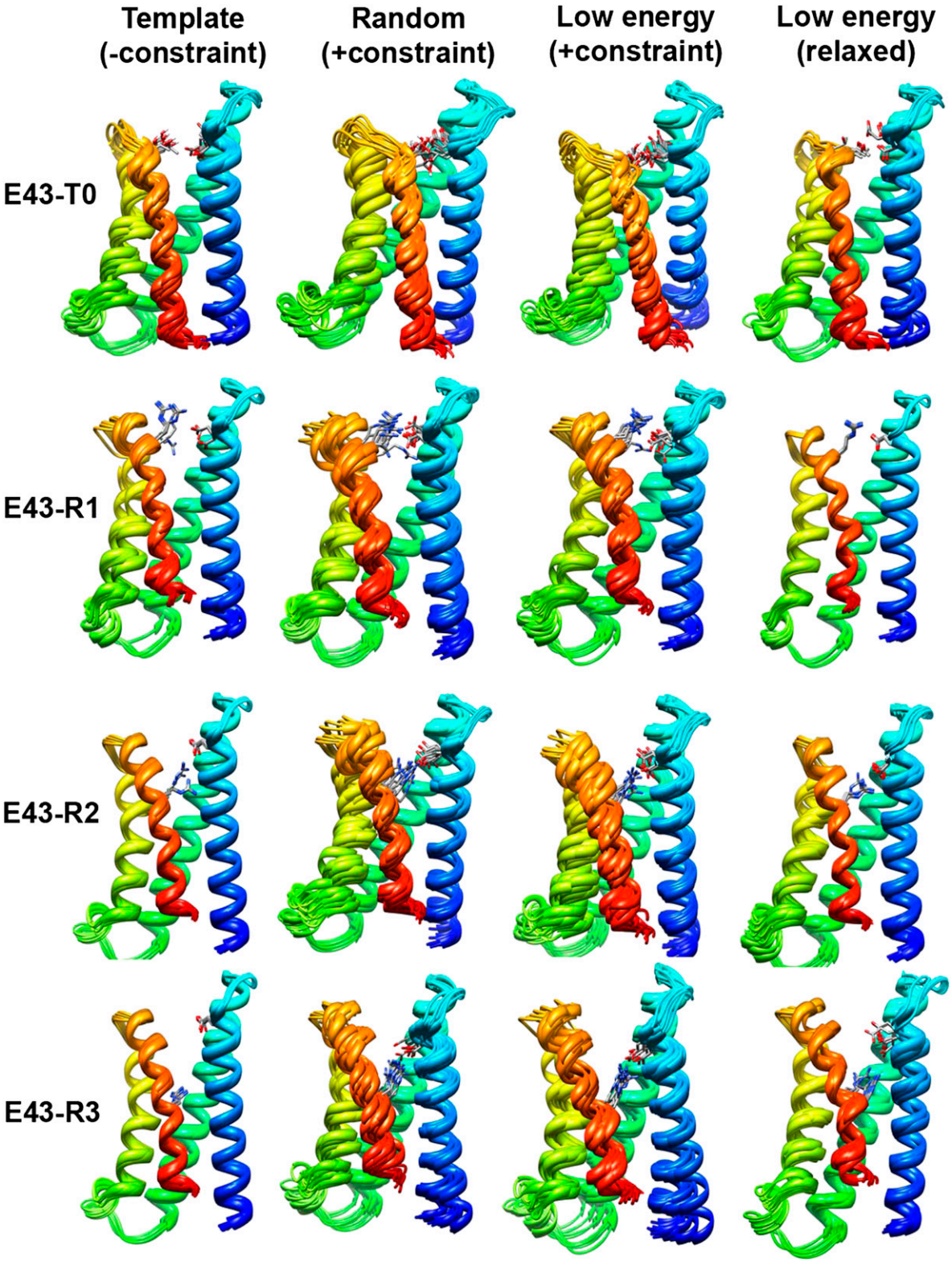

Fig. S7. Ensembles of NaChBac VSD models based on experimental constraints for E43-T0, E43-R1, E43-R2, and E43-R3 pairs. Transmembrane view of ensembles of Rosetta models of NaChBac VSD. The left-hand panel shows ensembles of ten lowest energy template-based models generated without experimental constraint. The second panel shows ensembles of ten random models generated with experimental constraint (indicated on the left side of the first panel). The third panel shows ensemble of ten lowest energy models generated with experimental constraint. The fourth (right-hand) panel shows ensembles of ten lowest energy models generated without experimental constraint from ten lowest energy models shown in the third panel. Segments S1 through S4 colored by a rainbow scheme from blue (S1) to green (S2) to yellow (S3) to orange-red (S4). Side chains of constrained residues are shown in stick representation and labeled. Gray, blue, and red atoms in the side chains represent carbon, nitrogen, and oxygen atoms, respectively.

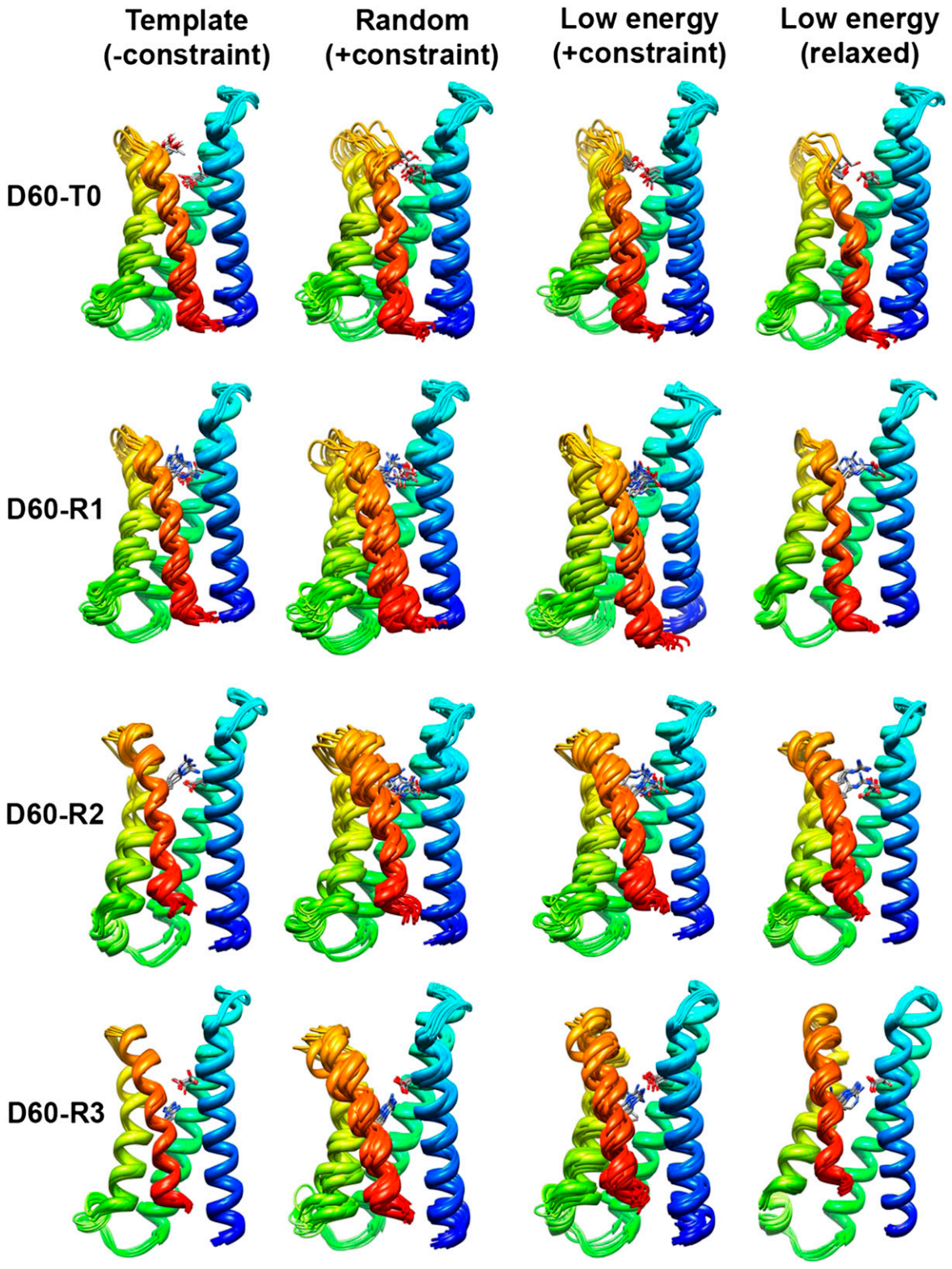

Fig. S8. Ensembles of NaChBac VSD models based on experimental constraints for D60-T0, D60-R1, D60-R2, and D60-R3 pairs. Transmembrane view of ensembles of Rosetta models of NaChBac VSD analogous to those of Fig. S7 but with the indicated constraints. Figure colored and labeled as in Fig. S7.

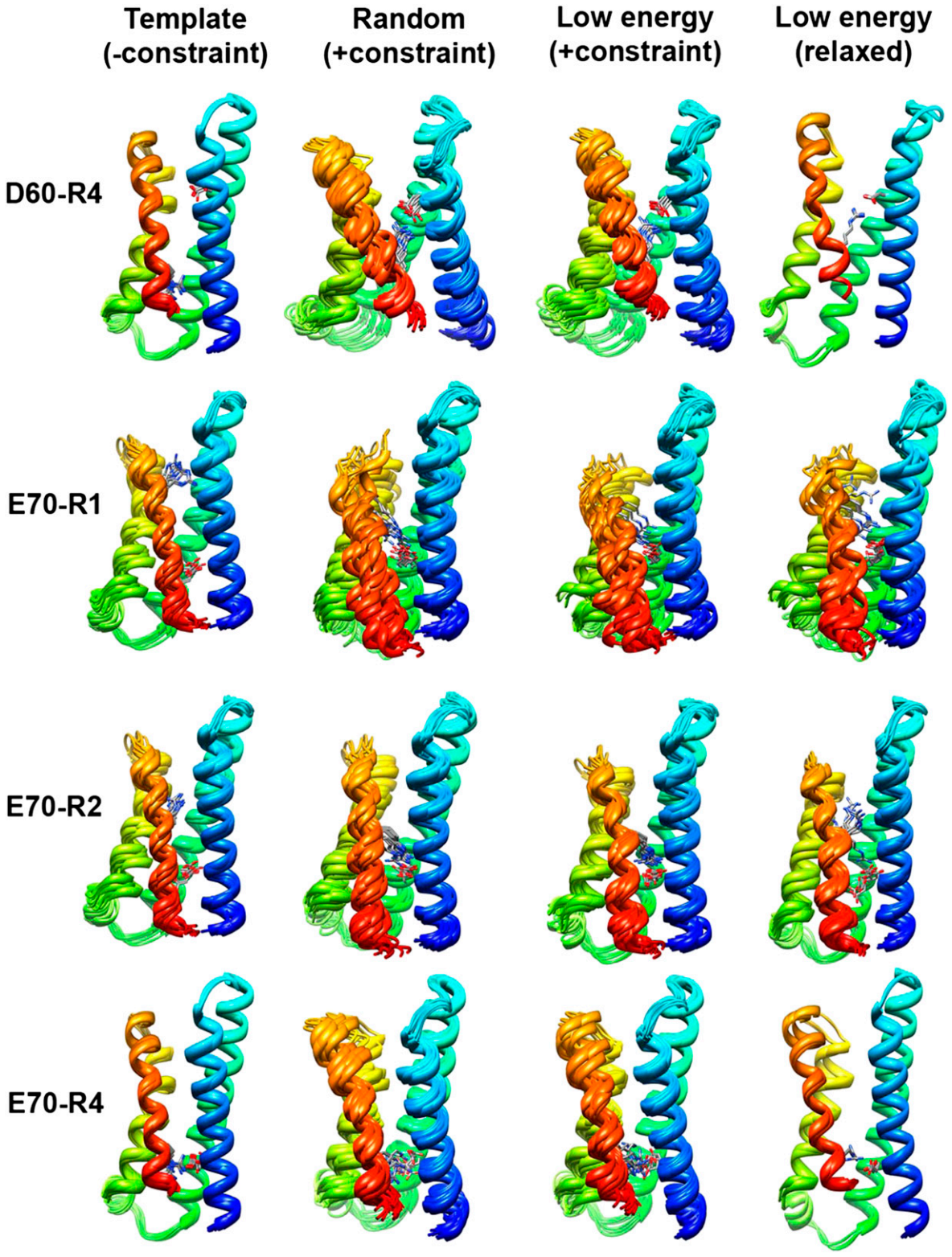

Fig. S9. Ensembles of NaChBac VSD models based on experimental constraints for D60-R4, E70-R1, E70-R2, and E70-R4 pairs. Transmembrane view of ensembles of Rosetta models of NaChBac VSD analogous to those of Fig. S7 but with the indicated constraints. Figure colored and labeled as in Fig. S7.

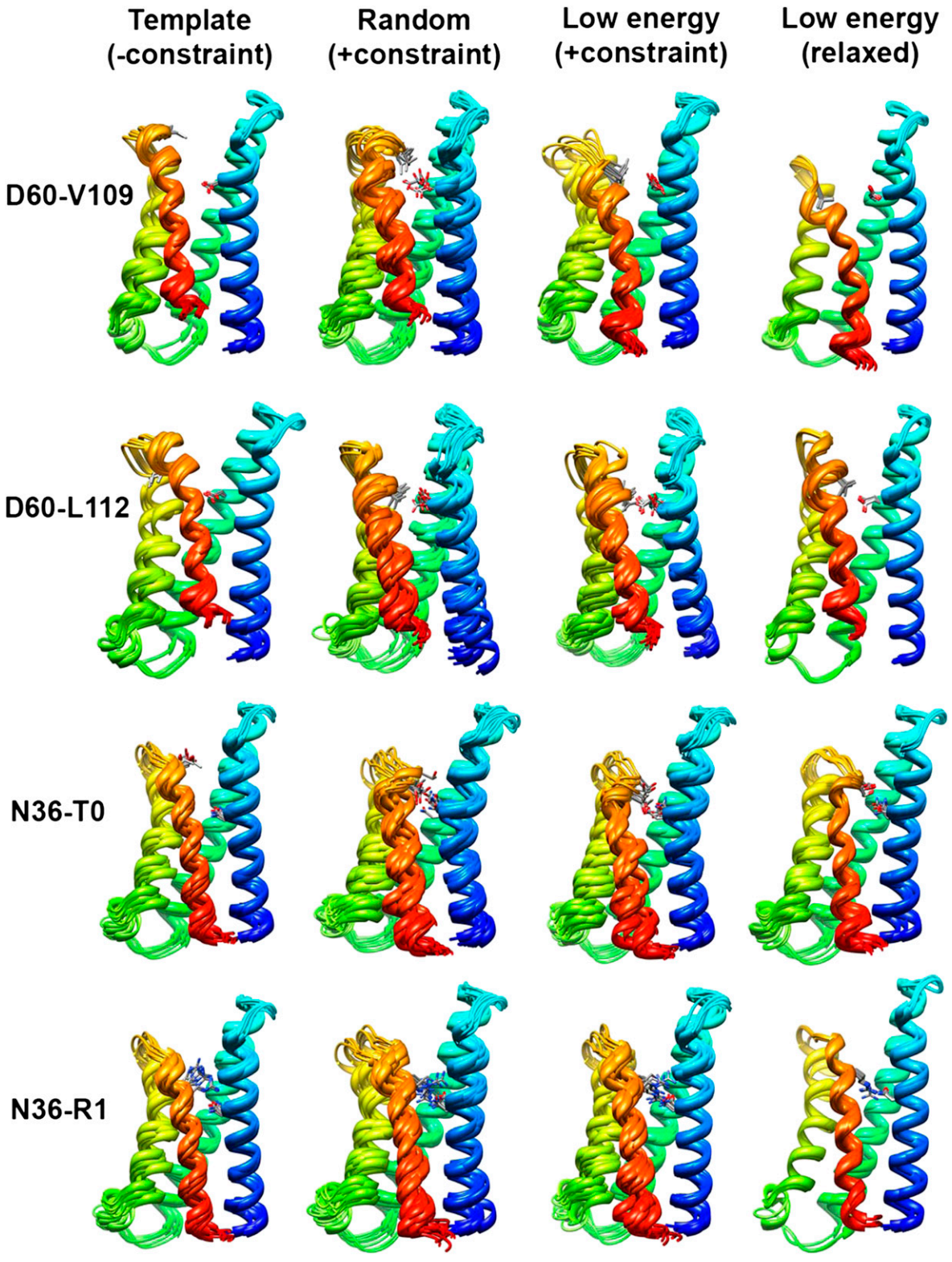

Fig. S10. Ensembles of NaChBac VSD models based on experimental constraints for D60-V109, D60-L112, N36-T0, and N36-R1 pairs. Transmembrane view of ensembles of Rosetta models of NaChBac VSD analogous to those of Fig. S7 but with the indicated constraints. Figure colored and labeled as in Fig. S7.

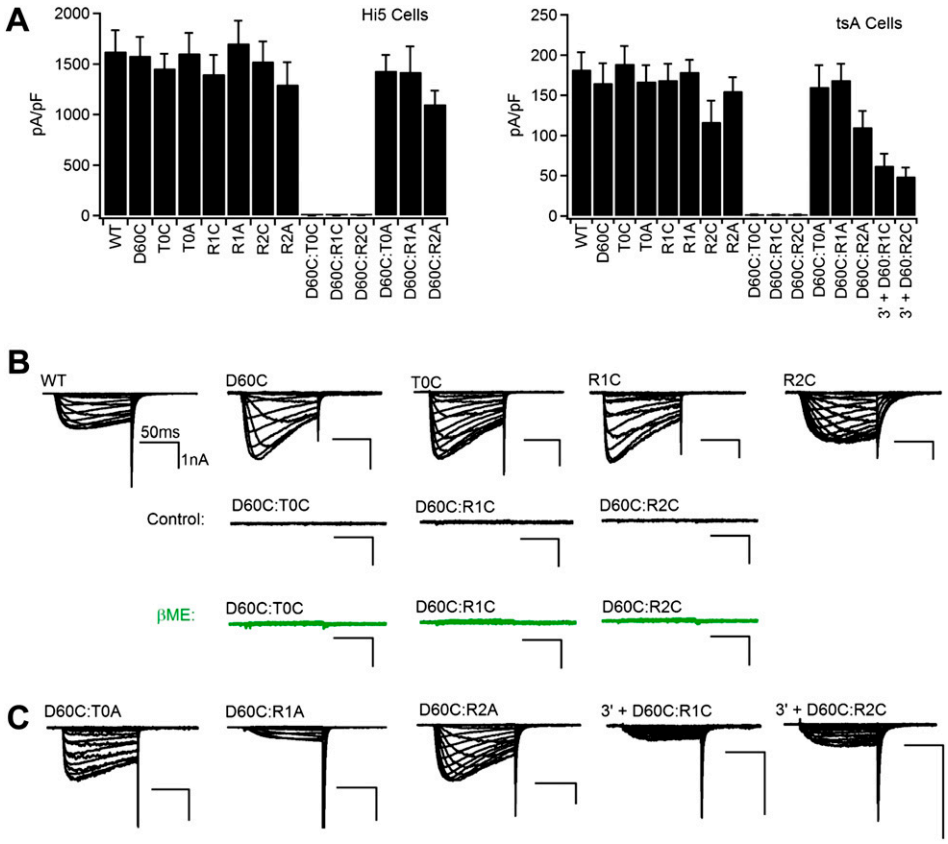

Fig. S11. Expression of WT and D60C double-cysteine mutants. (*A*) I_{Na} density from Hi5 insect cells infected with baculovirus (left) or tsA-201 cells transfected with cDNA (right). The expressed constructs encoded WT, D60C,T0C, T0A, R1C, R1A, R2C, R0A, D60C:T0C, D60C:R1C, D60C:R2C, D60C:T0A, D60C:R1A, D60C:R2A and trimer (3′) NaChBac channels. Current density calculated from I_{Na} at $V_{1/2}$ divided by the cell capacitance (± SEM). (*B*, *C*) Sodium currents elicited by 100-ms 10-mV steps from -140mV to 50 mV pulses from voltage clamped tsA-201 cells expressing the indicated NaChBac channels recorded in control conditions (black traces) and with 10 mM βME (green traces). 3′ + D60C:R1C and 3′ + D60C:R2C indicate cells transfected with cDNA plasmids encoding for double mutant monomers and a wild type trimer.

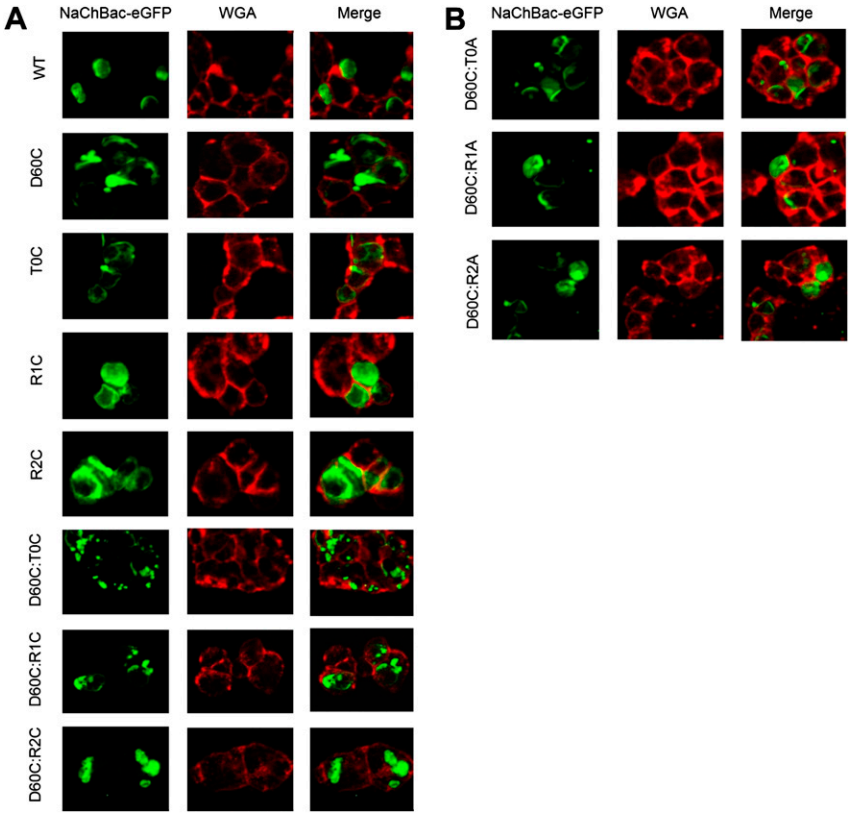

Fig. S12. Confocal images of wild-type and mutant NaChBac-eGFP. (*A*) cysteine single and double mutants and (*B*) cysteine-alanine single and double mutants. Cell membranes were stained for membrane carbohydrate with wheat germ agglutinin (WGA) in red and fixed using paraformaldehyde.

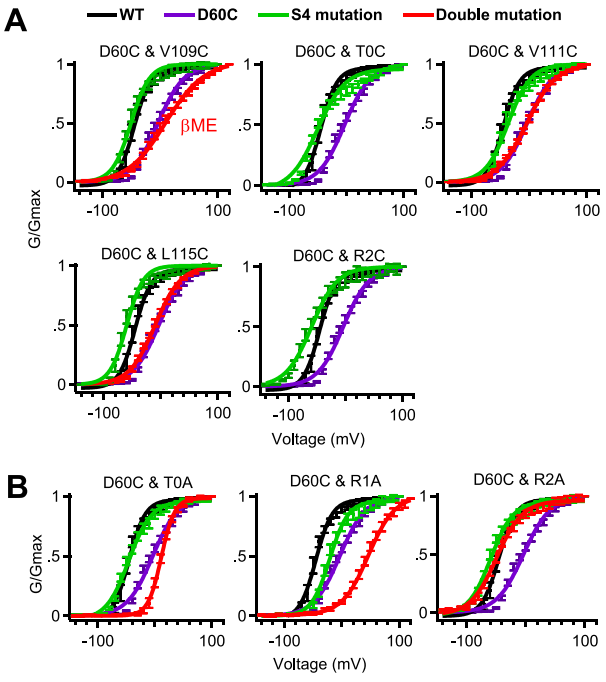

Fig. S13. Mutant cycle analysis of D60 interactions with gating charges and hydrophobic residues in the S4 segment. (*A*) Conductance-voltage relationships for WT, D60C, single cysteine mutants and double cysteine mutants of S4 residues as indicated. (*B*) WT, D60C, single alanine mutants, and double cysteine-alanine mutants of S4 residues as indicated.

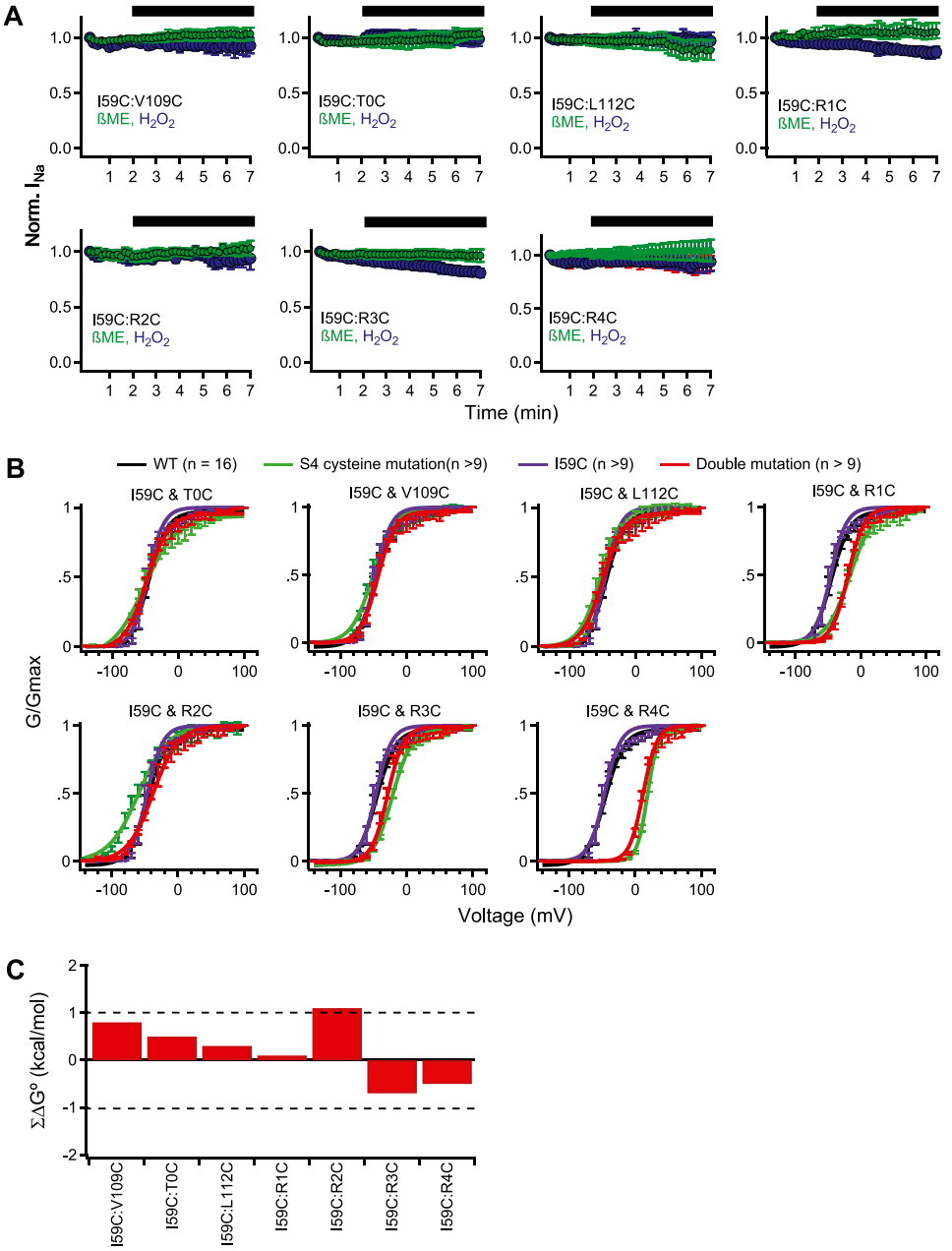

Fig. S14. Disulfide locking and mutant cycle analysis of double cysteine pairs with I59C. (*A*) Mean normalized peak I_{Na} elicited by 0.1 Hz trains of 500-ms depolarizations to $V_{1/2}$ +40 mV from a holding potential of -140 mV in cells expressing NaChBac I59C:V109C, I59C:T0C, I59C:L112C I59C:R1C, I59C:R2C, I59C:R3C and I59C:R4C channels. After 2 min in control saline, cells were exposed to either 2 mM H_2O_2 or 10mM βME for 5 min (black bars). Normalized I_{Na} from cells that were treated with βME are represented by blue circles and those treated with H_2O_2 are represented by green (*n* = 4 for each channel in each condition) (*B*) Conductance-voltage relationships are plotted for WT, double mutant channels and their component I59C and S4 single mutant channels. Conductance-voltage relationships were calculated from peak I_{Na} elicited by 100-ms depolarizations to the indicated potentials as described in *SI Methods* (number of cells tested is indicated in parentheses; ± SEM). (**C**) Results from mutant cycle analysis for double mutants I59C and S4 cysteine mutations. ΣΔG° is the nonadditive free energy or free energy coupling: the difference between the sum of the perturbation free energy of a double mutant channel containing both mutations and the perturbation free energies of the single mutant channels as described in *SI Methods*. Error = SEM.

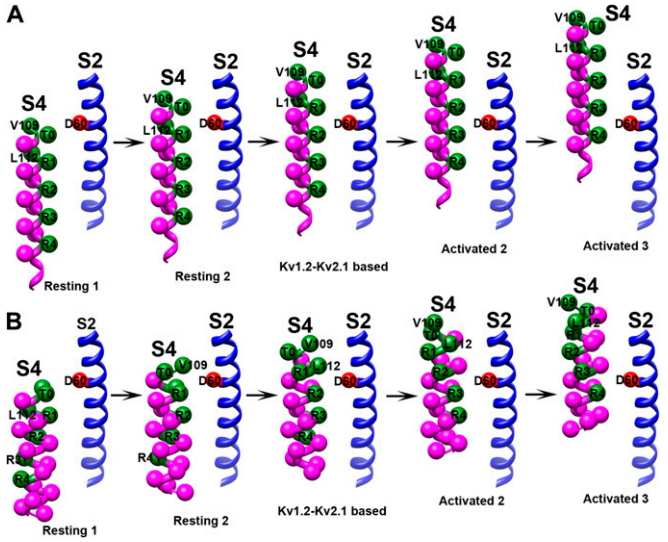

Fig. S15. Theoretical models of S4 structure and movement. (*A*) Illustration of S4 in 3_{10}-helical conformation. Five theoretical states of S4 are shown relative to D60 in S2. Cβ atoms of D60 (in S2) and S4 residues studied in this paper (from V109 to A123) are shown in space-filling representation. S4 residues that have been shown to be in close proximity to D60 by disulfide crosslinking and/or by coupling energy are colored in green and labeled. D60 in S2 is colored red. (*B*) Illustration of S4 in alpha-helical conformation. Five theoretical states of S4 are shown relative to D60 in S2. Residues colored and labeled as in panel *A*.

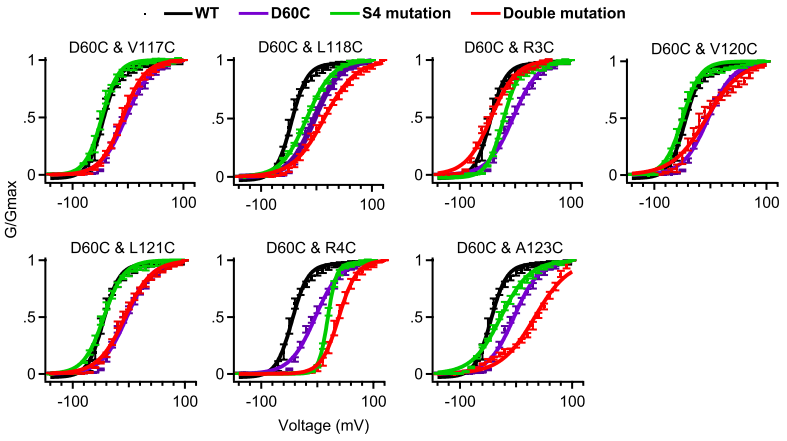

Fig. S16. Voltage dependence of activation for wild-type and mutant NaChBac. Conductance-voltage relationships are plotted for WT, D60C, single cysteine S4 mutations, and their double cysteine mutant channels as indicated. Conductance-voltage relationships were calculated from peak I_{Na} elicited by 100-ms depolarizations to the indicated potentials ($n > 9$; ± SEM) as described in *SI Methods*.

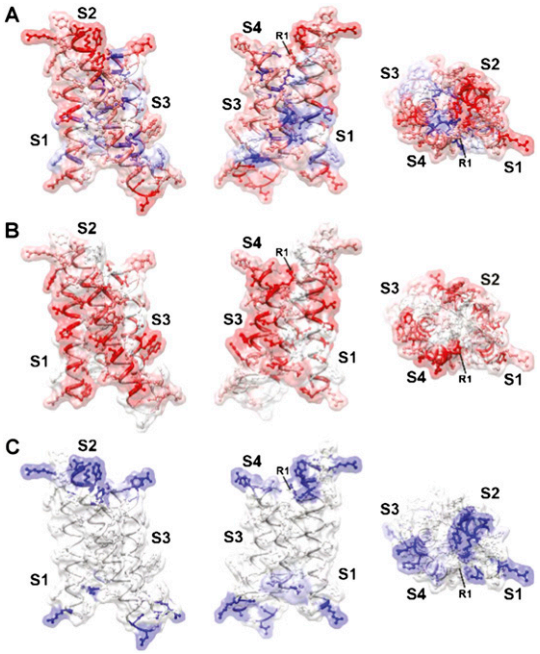

Fig. S17. EPR accessibility data mapped onto Kv1.2-Kv2.1-based model of the VSD of NaChBac. EPR data environmental parameters ΔH_o^{-1} (*A*), ΠO_2 (*B*), and ΠNiEdda (*C*) (33) mapped onto cartoon, ball and stick, and molecular surface representation of VSD of NaChBac. Left column shows transmembrane view of the model with S1, S2, and S3 segments on the front. Middle column shows transmembrane view of the model with S1, S3, and S4 segments on the front. Right column shows extracellular view of the model. Position of the first gating charge-carrying arginine in S4 indicated by black line and labeled. Individual residues are colored as in Fig. 4 of Chakrapani et al. (33).

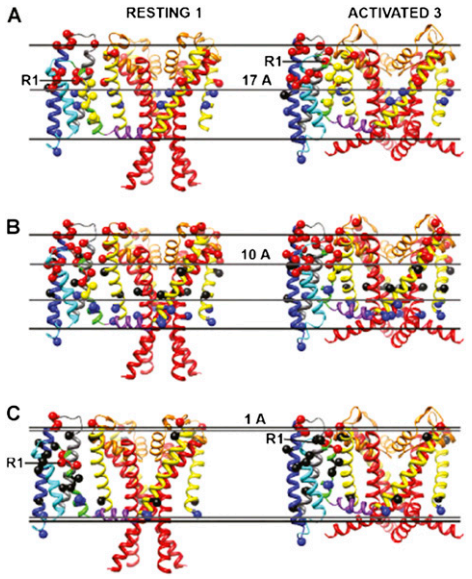

Fig. S18. Biotin-avidin accessibility data mapped onto Resting State 1 and Activated State 3 models of NaChBac. The avidin accessibility of the KvAP residues to biotin attachments of different length (34) mapped onto a single domain of VSD and four domains of PD of NaChBac and shown from the side of the membrane. Transmembrane segment S1 colored gray and segments S2 through S6, and P-loop colored by rainbow scheme from blue to red and shown in ribbon representation. Black bars indicate approximate location of the extracellular and intracellular edges of ~34 Å wide membrane layer. Gray lines indicate 17 Å (top panel), 10 Å (middle panel), and 1 Å (bottom panel) vertical distance from the extracellular and intracellular edges of the membrane. Cβ carbon atoms of NaChBac residues that correspond to KvAP residues studied by Ruta et al. (34) (according to sequence alignment shown in Fig. S1) shown as spheres and colored as follows: red – residues that are accessible to avidin only from the extracellular side of the membrane; yellow – residues that are accessible to avidin from both sides of the membrane; black - residues that are inaccessible; blue - residues that are accessible to avidin only from the intracellular side of the membrane.

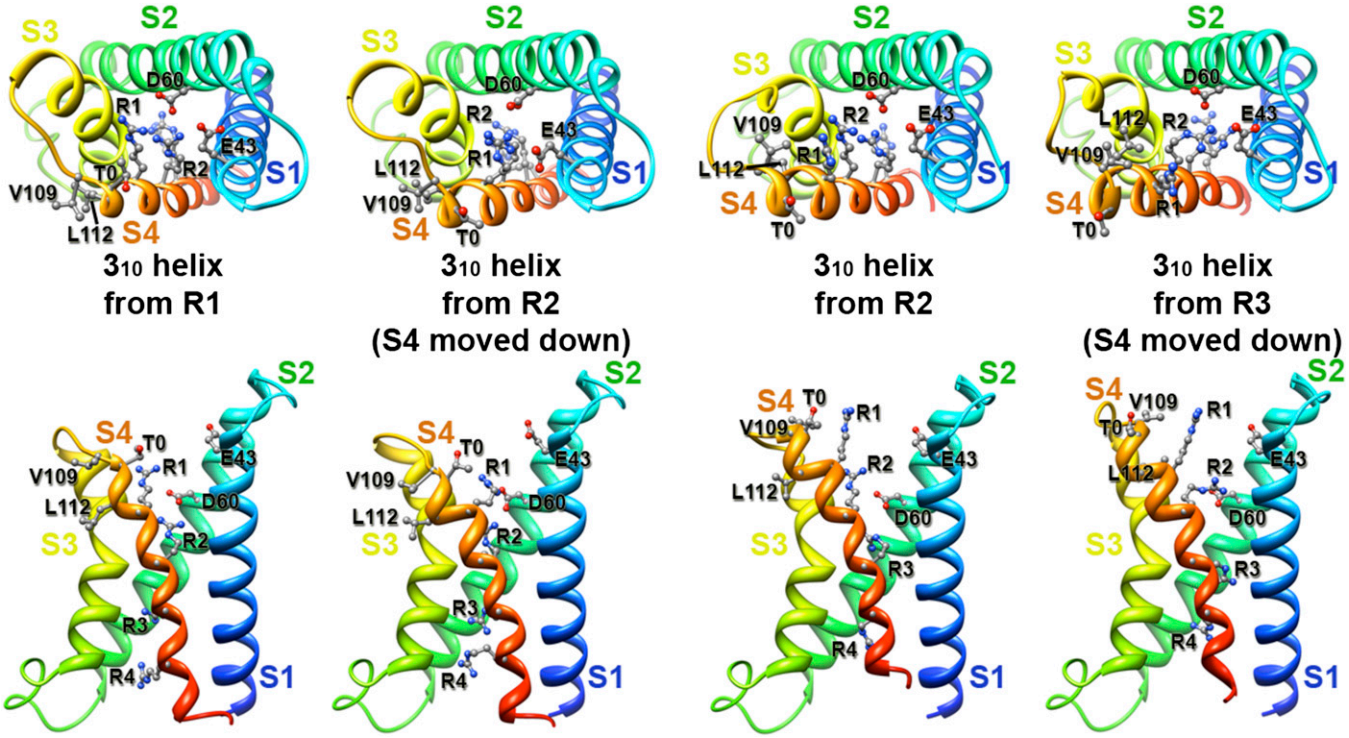

Fig. S19. Starting templates for NaChBac VSD modeling based on different S4 alignments. The S1-S3 segments of NaChBac were modeled based on S1-S3 segment of Kv1.2-Kv2.1 chimera structure (5) using sequence alignments shown in Fig. S1. The S4 segment of NaChBac was modeled based on S4 segment of Kv1.2-Kv2.1 chimera structure (5) using sequence alignments shown in Fig. S5. "3_{10} helix from R1" starting template is based on S4 alignment shown in Fig. S5*C*. "3_{10} helix from R2 (S4 moved down)" starting template is based on S4 alignment shown in Fig. S5*B* and in which S4 coordinates were shifted by one helix turn down. "3_{10} helix from R2" starting template is based on S4 alignment shown in Fig. S5*B*. "3_{10} helix from R3 (S4 moved down)" starting template is based on S4 alignment shown in Fig. S5*A* and in which S4 coordinates were shifted by one helix turn down. Segments S1 through S4 colored by a rainbow scheme from blue (S1) to green (S2) to yellow (S3) to orange (S4). Side chains of key residues in VSD of NaChBac are shown in ball and stick representation and labeled.

Table S1. Voltage dependence of conductance parameters, calculated free energy of activation and perturbation of free energy values of single mutant channels

Channel	Z	$V_{1/2}$	ΔG°	ΔΔG°
Wt	3.7 ± 0.2	−43 ± 2	−3.8 ± 0.2	—
I59C	3.8 ± 0.2	−46 ± 2	−4.0 ± 0.2	−0.2
D60C	2.7** ± 0.2	−19** ± 2	−1.2 ± 0.2	2.6
V109C	3.7 ± 0.1	−48** ± 3	−4.1 ± 0.2	−0.3
T0A (T110A)	3.0** ± 0.2	−49** ± 2	−3.4 ± 0.2	0.4
T0C (T110C)	2.9** ± 0.2	−47* ± 2	−3.1 ± 0.2	0.7
V111C	3.3 ± 0.2	−42 ± 3	−3.2 ± 0.2	0.6
L112C	3.6 ± 0.2	−51* ± 3	−4.1 ± 0.2	−0.3
R1A (R113A)	3.4 ± 0.2	−25** ± 3	−1.9 ± 0.2	1.8
R1C (R113C)	3.0** ± 0.1	−19** ± 3	−1.3 ± 0.2	2.5
I114C	3.0* ± 0.2	−31** ± 2	−2.2 ± 0.2	1.7
L115C	3.4 ± 0.2	−65** ± 2	−5.1 ± 0.2	−1.3
R2A (R116A)	3.0** ± 0.3	−55* ± 3	−3.8 ± 0.3	0.0
R2C (R116C)	2.9* ± 0.2	−63** ± 3	−4.2 ± 0.3	−0.4
V117C	2.7 ± 0.2	−44 ± 2	−2.8 ± 0.2	1.0
L118C	2.8** ± 0.3	−19** ± 3	−1.2 ± 0.3	2.6
R3C (R119C)	3.0** ± 0.2	−25** ± 2	−1.7 ± 0.2	2.1
V120C	3.0** ± 0.3	−50** ± 3	−3.5 ± 0.3	0.3
L121C	3.4 ± 0.2	−43 ± 2	−3.4 ± 0.2	0.4
R4C (R122C)	4.1* ± 0.2	17** ± 2	1.6 ± 3	5.4
A123C	2.9* ± 0.3	−30** ± 3	−2.0 ± 0.3	1.8

Measured G-V relationships for the WT and mutant NaChBac channels were fit with a Boltzmann equation and values for Z and $V_{1/2}$ in mV are tabulated (see *SI Methods*). ΔG° = $ZV_{1/2}$*0.02306, the free energy (kcal/mol) required to shift the channel from the closed to open state at 0 mV. ΔΔG° (kcal/mol) is the perturbation free energy of the mutant channel relative to WT. Error = SEM.

Table S2. Parameters and calculated free energy values supporting mutant cycle analysis

Channel	Z	$V_{1/2}$	ΔG°	ΔΔG°	ΣΔG°
D60C:V109C	2.5 ± 0.2	8 ± 2	0.5 ± 0.2	4.3	2.0
D60C:T110A	3.7 ± 0.2	11 ± 2	1.0 ± 0.2	4.8	1.8
D60C:T110C			No membrane expression		
D60C:V111C	2.7 ± 0.2	−15 ± 2	−0.9 ± 0.2	2.9	−0.3
D60C:L112C	3.4 ± 0.2	−55 ± 2	−4.3 ± 0.2	−0.5	−2.7
D60C:R113A	2.8 ± 0.2	31 ± 2	2.0 ± 0.2	5.8	1.4
D60C:R113C			No membrane expression		
D60C:I114C	2.7 ± 0.3	15 ± 2	0.9 ± 0.3	4.7	0.5
D60C:L115C	3.1 ± 0.2	−27 ± 2	−1.9 ± 0.3	1.9	0.6
D60C:R116A	3.0 ± 0.2	−45 ± 2	−3.1 ± 0.2	0.7	−1.9
D60C:R116C			No membrane expression		
D60C:V117C	2.8 ± 0.2	−13 ± 3	−0.9 ± 0.2	2.9	−0.7
D60C:L118C	2.8 ± 0.3	18 ± 2	1.1 ± 0.2	4.9	−0.2
D60C:R119C	2.5 ± 0.2	−51 ± 3	−2.9 ± 0.2	0.9	−3.8
D60C:V120C	2.4 ± 0.3	−26 ± 2	−1.5 ± 0.3	2.3	−0.6
D60C:L121C	2.8 ± 0.2	−24 ± 3	−1.5 ± 0.2	2.2	−0.7
D60C:R122C	2.9 ± 0.3	36 ± 3	2.4 ± 0.2	6.2	−1.7
D60C:A123C	1.6 ± 0.2	31.9 ± 0.3	1.2 ± 0.2	5.0	−0.6
I59C:V109C	3.6 ± 0.2	−44 ± 3	−3.7 ± 0.2	0.1	0.8
I59C:T110C	3.2 ± 0.2	−44 ± 3	−3.6 ± 0.2	0.2	0.5
I59C:L112C	3.4 ± 0.2	−52 ± 2	−4.3 ± 0.2	−0.5	0.3
I59C:R113C	3.5 ± 0.2	−19 ± 2	−1.5 ± 0.2	2.3	0.1
I59C:R116C	3.1 ± 0.2	−48 ± 2	3.3 ± 0.2	0.5	1.1
I59C:R119C	3.5 ± 0.2	−34 ± 2	−2.7 ± 2	1.1	−0.7
I59C:R122C	3.7 ± 0.2	9 ± 2	0.8 ± 0.2	4.6	−0.5

Measured G-V relationships for the WT and mutant NaChBac channels were fit with a Boltzmann equation and values for Z and $V_{1/2}$ in mV are tabulated (see *SI Methods*). ΔG° = $ZV_{1/2}$*0.02306, the free energy (kcal/mol) required to shift the channel from the closed to open state at 0 mV. ΔΔG° (kcal/mol) is the perturbation free energy of the mutant channel relative to WT. ΣΔG° is the nonadditive free energy or free energy coupling: the difference between perturbation free energy of a double mutant channel containing both mutations and the sum of the perturbation free energies of the single mutant channels. Error = SEM.

Table S3. Distances between Cβ atoms of D60 (in S2) and residues in S4 (in Å) for all NaChBac structural models presented in the main text

	Model								
Residue pair	R1	R2	R3	Kv1.2–2.1	A1	A2	A3	Minimum distance	Observed interaction
D60-V109	8	12	11	10	10	11	13	8	+
D60-T0	5	9	14	13	14	15	17	5	+
D60-V111	10	13	12	14	14	15	17	10	-
D60-L112	11	13	7	9	9	10	12	7	+
D60-R1	8	8	11	9	9	10	12	8	+
D60-I114	13	13	14	13	13	14	16	13	-
D60-L115	14	14	11	12	12	13	14	11	-
D60-R2	10	10	7	8	7	8	9	7	+
D60-V117	15	15	13	13	13	13	14	13	-
D60-L118	17	16	13	14	13	14	14	13	-
D60-R3	17	15	10	10	10	10	9	9	+
D60-V120	19	19	15	15	15	14	15	14	-
D60-L121	22	21	16	17	16	16	14	16	-
D60-R4	22	20	14	15	14	13	10	10	+
D60-A123	22	21	18	18	18	17	15	15	-

Distances between Cβ atoms of D60 (in S2) and residues in S4 (in Angstroms) for all NaChBac structural models presented in the main text, Resting (R) 1 through 3, KV1.2–2.1, and Activated (A) 1 through 3. Underlined residue pairs have been shown to be in close proximity either by disulfide crosslinking and/or by coupling energy (see Fig. 7*A–C*).

Table S4. Distances between Cβ atoms of D60 (in S2) and residues in S4 (in Å) for S4 in all 3_{10}-helical conformation

	Model						
Residue Pair	R1 (D60–T0)	R2 (D60–R1)	Kv1.2–2.1 (D60–R2)	A2 (D60–R3)	A3 (D60–R4)	Minimum distance	Observed interaction
D60-V109	11	13	16			11	+
D60-T0	7	8	12			7	+
D60-V111	13	12	14			12	-
D60-L112	13	11	13	16		11	+
D60-R1	11	7	8	12		7	+
D60-I114	16	13	12	14		12	-
D60-L115	16	13	11	13	16	11	-
D60-R2	16	11	7	8	12	7	+
D60-V117	20	16	13	12	14	12	-
D60-L118		16	13	11	13	11	-
D60-R3		16	11	7	8	7	+
D60-V120		20	16	13	12	12	-
D60-L121			16	13	11	11	-
D60-R4			16	11	7	7	+
D60-A123			20	16	13	13	-

Distances between Cβ atoms of D60 (in S2) and residues in S4 (in Angstroms) for S4 in all 3_{10} conformation, for models based on the indicated constraints. Underlined residue pairs have been shown to be in close proximity either by disulfide crosslinking and/or by coupling energy (see Fig. 7*A–C*).

Table S5. Distances between Cβ atoms of D60 (in S2) and residues in S4 (in Å) for S4 in all alpha-helical conformation

	Model						
Residue Pair	R1 (D60–T0)	R2 (D60–R1)	Kv1.2–2.1 (D60–R2)	A2 (D60–R3)	A3 (D60–R4)	Minimum distance	Observed interaction
D60-V109	9	7	11			9	+
D60-T0	8	11	14			8	+
D60-V111	13	13	12			12	-
D60-L112	13	9	7	11		7	+
D60-R1	10	8	11	14		8	+
D60-I114	13	13	13	12		12	-
D60-L115	17	13	9	7	11	7	-
D60-R2	16	10	8	11	14	8	+
D60-V117	15	13	13	13	12	12	-
D60-L118		17	13	9	7	7	-
D60-R3		16	10	8	11	8	+
D60-V120		15	13	13	13	13	-
D60-L121			17	13	9	9	-
D60-R4			16	10	8	8	+
D60-A123			15	13	13	13	-

Distances between Cβ atoms of D60 (in S2) and residues in S4 (in Angstroms) for S4 in all alpha conformation, for models based on the indicated constraints. Underlined residue pairs have been shown to be in close proximity either by disulfide crosslinking and/or by coupling energy (see Fig. 7*A–C*).

Table S6. Comparison of NaChBac VSD Structural Models with Experimental Data

State	Experimental constraint	Additional supporting data
Resting 1	N36.CG – T0.CB = 3.6 ± 0.3 Å (35)	Avidin-biotin (34) Cell growth complementation (33) Gating pore current (36–39) Second-site suppressor (40)
Resting 2	E43.CG – T0.CB = 3.6 ± 0.3 Å (17)	Disulfide crosslinking (41) Cell growth complementation (33) Gating pore current (36–39) Mg^{2+} binding (42) Double mutant cycle (43) Second-site suppressor (40, 44, 45)
Resting 3	D60.CB – L112.CB = 6.0 ± 0.3 Å (17)	Disulfide crosslinking (17) Gating pore current (38, 39) Double mutant cycle (43) Second-site suppressor (40, 44, 45)
Kv1.2-Kv2.1 structure based	none	Disulfide crosslinking (17, 46, 47) Double mutant cycle (43) EPR spectroscopy (33) Second-site suppressor (40, 44, 45)
Activated 1	E43.CD – R2.CZ = 4.2 ± 0.2 Å (17)	Disulfide crosslinking (17, 46, 47) Gating pore current (38, 39) Double mutant cycle (43) EPR spectroscopy (33) Second-site suppressor (40, 44, 45)
Activated 2	D60.CG – R3.CZ = 4.2 ± 0.2 Å (47)	Disulfide crosslinking (46) EPR spectroscopy (33) Gating pore current (38, 39) Second-site suppressor (40, 44, 45)
Activated 3	D60.CG – R4.CZ = 4.2 ± 0.2 Å (46)	Disulfide crosslinking (17) Double mutant cycle (43) Avidin-biotin (34) EPR spectroscopy (33)

The "Experimental constraint" column shows experimental distance constraints used to generate structural models of individual states. The "Additional supporting data" column shows experimental data that support structural models of individual states. All of our *Activated State* models fit very well with EPR spectroscopy data for the isolated VSD of NaChBac (Fig. S17) (33). Our *Activated State 1* model fits with disulfide-locking results showing that R2 interacts with E43 (in S1), R3 interacts with D60 (in S2), and R4 interacts with E70 (in S2) in the activated state of the VSD of NaChBac (46–48) and with mutant cycle analysis data showing that E43 (in S1) and R2 are energetically coupled (43). Our *Activated State 2* model fits with disulfide-locking and genetic complementation data showing that R2 interacts with E43 (in S1) and R3 interacts with D60 (in S2) in the activated state of the VSD of NaChBac (46–48) and that the corresponding residues interact in Shaker K_V channels (40, 44, 45). Our *Resting State 1* model is in agreement with biotin-avidin accessibility data for the KvAP channel (34, 49) (Fig. S18), and further significant inward movement of S4 would put R1 within ~17 Å from the intracellular side of the membrane and would be in disagreement with these experimental data. The R1 and R2 side chains form the major barrier for ion leak through the VSD in our *Resting State 1* and *2* models, which is in agreement with genetic complementation data on the NaChBac channel showing that R1G and R2G mutations conduct potassium in the resting state (33), and with gating pore current data showing that the R1Q/R2Q double mutant in VSD of domain II of the $Na_V1.2$ channel (38) and R1S in the *Shaker* K_V channel conduct ionic leak current in the resting state (36, 37, 39). The close proximity between *Shaker* I287 (L64 in S2 of NaChBac) and F324 (H101 in S3 of NaChBac) in the resting state was suggested based on Mg^{2+} binding to I287D and F324D (42). The corresponding Cβ-Cβ distance between L64 (in S2) and H101 (in S3) is ~6 Å in our model, compatible with formation of Mg^{2+} binding site by aspartates at these positions. Our *Resting State 2* model is in agreement with disulfide bond between I325C (I102 in S3 of NaChBac) and I360C (F108 in S3-S4 loop of NaChBac) in *Shaker* (41). Our models for *Resting State 1* and *2* are also supported by double-mutant cycle analysis results and genetic complementation studies showing that R1 and E43 (in S1) (43), R1 and D60 (in S2), and R2 and D60 (in S2) are energetically coupled and that the corresponding residues interact in Shaker K_V channels (40, 44, 45).